Impacts of microphysical scheme on convective and stratiform characteristics in two high precipitation squall line events

Di Wu,[1,2] Xiquan Dong,[1] Baike Xi,[1] Zhe Feng,[1,3] Aaron Kennedy,[1] Gretchen Mullendore,[1] Matthew Gilmore,[1] and Wei-Kuo Tao[2]

Received 13 November 2012; revised 23 August 2013; accepted 27 August 2013; published 4 October 2013.

[1] This study investigates the impact of snow, graupel, and hail processes on simulated squall lines over the Southern Great Plains in the United States. The Weather Research and Forecasting (WRF) model is used to simulate two squall line events in Oklahoma during May 2007, and the simulations are validated against radar and surface observations. Several microphysics schemes are tested in this study, including the WRF 5-Class Microphysics (WSM5), WRF 6-Class Microphysics (WSM6), Goddard Cumulus Ensemble (GCE) Three Ice (3-ice) with graupel, Goddard Two Ice (2-ice), and Goddard 3-ice hail schemes. Simulated surface precipitation is sensitive to the microphysics scheme when the graupel or hail categories are included. All of the 3-ice schemes overestimate the total precipitation with WSM6 having the largest bias. The 2-ice schemes, without a graupel/hail category, produce less total precipitation than the 3-ice schemes. By applying a radar-based convective/stratiform partitioning algorithm, we find that including graupel/hail processes increases the convective areal coverage, precipitation intensity, updraft, and downdraft intensities, and reduces the stratiform areal coverage and precipitation intensity. For vertical structures, simulations have higher reflectivity values distributed aloft than the observed values in both the convective and stratiform regions. Three-ice schemes produce more high reflectivity values in convective regions, while 2-ice schemes produce more high reflectivity values in stratiform regions. In addition, this study has demonstrated that the radar-based convective/stratiform partitioning algorithm can reasonably identify WRF-simulated precipitation, wind, and microphysical fields in both convective and stratiform regions.

Citation: Wu, D., X. Dong, B. Xi, Z. Feng, A. Kennedy, G. Mullendore, M. Gilmore, and W.-K. Tao (2013), Impacts of microphysical scheme on convective and stratiform characteristics in two high precipitation squall line events, *J. Geophys. Res. Atmos.*, *118*, 11,119–11,135, doi:10.1002/jgrd.50798.

1. Introduction

[2] With the advancement of microphysics schemes, extensive validations for existing schemes are needed in order to constrain and reduce any uncertainties. The current validation techniques depend upon the availability of observations. In situ measurements are essential for detailed and direct microphysics validations, such as particle size distributions and liquid/ice water content. However, these observations are limited to certain field campaigns as well as certain parts of the storms. On the other hand, radar and rain gauge measurements are widely available for the continental United States. Radar reflectivity provides the bulk information of 3-D distributions of hydrometeors and is very useful in model validations.

[3] A mesoscale convective system (MCS) primarily consists of convective and stratiform regions [*Houze*, 1977], where significantly different microphysical and thermodynamic features are observed. In convective regions, the growth of ice is dominated by riming, whereas in stratiform regions, deposition and aggregation are the primary mechanisms [*Churchill and Houze*, 1984]. The resultant latent heating profiles are quite different for the two regions [e.g., *Leary and Houze*, 1979; *Houze*, 1982; *Tao et al.*, 1989]. Previous studies have shown many discrepancies between models and observations, such as smaller stratiform areal coverage and weaker precipitation [*Fovell and Ogura*, 1988; *McCumber et al.*, 1991; *Luo et al.*, 2010], and heavier precipitation from convective regions [e.g., *Luo et al.*, 2010] in simulated storms. The simulated storm structure is known to be sensitive to the choice of the microphysics schemes. Double-moment schemes have previously been shown to produce more accurate precipitation compared with single-moment schemes [*Morrison et al.*, 2009; *Li et al.*, 2009]. Bin microphysics can produce a more realistic horizontally homogeneous stratiform region, whereas anomalous multicellular convective features

[1]Department of Atmospheric Sciences, University of North Dakota, Grand Forks, North Dakota, USA.
[2]NASA Goddard Space Flight Center, Greenbelt, Maryland, USA.
[3]Pacific Northwest National Laboratory, Richland, Washington, USA.

Corresponding author: X. Dong, Department of Atmospheric Sciences, University of North Dakota, 4149 University Ave. Stop 9006, Grand Forks, ND 58202-9006, USA. (dong@aero.und.edu)

2169-897X/13/10.1002/jgrd.50798

can appear within the stratiform region when using bulk microphysics [*Li et al*., 2009, 2009a]. Most importantly, different configurations of ice particles have shown large impacts on storm precipitation distributions [e.g., *Gilmore et al*., 2004a, 2004b], fallouts [e.g., *Cotton et al*., 1982; *McCumber et al*., 1991; *Ferrier et al*., 1995], updraft intensities [*Johnson et al*., 1993], downdraft intensities [e.g., *Proctor*, 1988, 1989; *Straka and Anderson*, 1993], and latent heat release [e.g., *Tao et al*., 2007].

[4] Despite limitations in current cloud-resolving models, the aforementioned model-observation discrepancies can also be partly attributable to differences in convective/stratiform partitioning algorithms and storm environment [*Lang et al*., 2003]. For objective model-observation comparisons, the convective/stratiform partitioning algorithms should be applied consistently. Many studies have used precipitation intensity as a measure to distinguish the convective from the stratiform regions [e.g., *Morrison et al*., 2009; *Li et al*., 2009, 2009a]. The theoretical background was based on *Houze* [1973] and *Churchill and Houze* [1984], where a given threshold precipitation intensity was used to identify convective precipitation. On the other hand, the separation of the convective and stratiform regions using radar has been well established [*Steiner et al*., 1995; *Feng et al*., 2011], and the algorithm has led to a better characterization of the precipitation structure of MCSs [*Lang et al*., 2003; *Houze*, 2004]. To date, there have not been many studies using this technique in model validations. Recently published papers include *Luo et al*. [2010], which focused on the Mei-yu front over east China, and *Varble et al.* [2011], which studied tropical convection over Darwin, Australia during the Tropical Warm Pool International Cloud Experiment (TWP–ICE). The purpose of this study is to apply this methodology to evaluate the impact of 2-ice schemes (cloud ice and snow processes) and 3-ice schemes (cloud ice, snow, graupel/hail) on simulated midlatitude continental MCS structures over the Southern Great Plains (SGP) of the United States. We investigate two squall line events over Oklahoma during May–July 2007 through the analysis of Next-Generation Radar (NEXRAD), Oklahoma Mesonet surface precipitation observations, and the WRF simulations. The data and methodology are described in sections 2 and 3, while results are presented in section 4. Conclusions are given in section 5.

2. Data Sources

[5] The data sets used in this study consist of North American Regional Reanalysis (NARR) as well as NEXRAD radar and Mesonet observations in Oklahoma. NARR is a regional reanalysis based on the NCEP ETA model, with 3 h temporal, 32 km horizontal, and 45 layer vertical resolutions over the North American domain since 1979 [*Mesinger et al*., 2006]. It is suitable for diagnosis of synoptic and mesoscale conditions over the State of Oklahoma. An assessment of NARR at the ARM SGP site has shown good agreement with atmospheric soundings [*Kennedy et al*., 2011]. In this study, the 500 hPa geopotential height and wind fields, surface mean sea level pressure, winds, temperature, and dew point temperature derived from NARR are used to explore the large-scale synoptic patterns of the two selected squall line cases.

[6] Radar reflectivity data from three NEXRAD radars (KTLX, KINX, KVNX) covering most of Oklahoma are used for this study. The radars operate at the wavelength of 10 cm (S band) in a preprogrammed sequence of 360° azimuthal sweeps at various elevation angles [*Klazura and Imy*, 1993]. A quality-control algorithm developed at the University of Washington [*Houze et al*., 2004] is applied to the radar data to remove echo clutter and anomalous propagation. NEXRAD data are interpolated on 3 km grid in order to match the resolution of the model grid.

[7] Surface precipitation measurements are obtained from the Oklahoma Mesonet, a statewide monitoring network that consists of over 110 automated weather stations covering the entire state of Oklahoma [*Brock et al*., 1995]. The Oklahoma Mesonet is a system designed to measure the environment at the size and duration of mesoscale weather events. In this study, the 5 min data from tipping bucket rain gauges are used for evaluating the WRF-simulated precipitation.

3. Simulation Design and Analysis Method

[8] Simulations of the two selected squall line events are conducted using the Advanced Research WRF model version 3.1.1. [*Skamarock et al*., 2008]. There are 40 vertical levels and two spatial domains in the simulations: 9 km for the outer domain and 3 km for the inner domain (Figure 1). The time periods of simulations are from 00Z 06 May to 00Z 08 May 2007 for Case 1 and from 00Z 23 May to 00Z 25 May 2007 for Case 2. The model initial and boundary conditions are provided by NARR, where the time-varying lateral boundary conditions are applied at 3 h intervals.

[9] The Kain-Fritsch convective parameterization scheme [*Kain*, 2004] is adopted for the outer domain; no convective parameterization was used for the inner domain. The other physical parameterizations used in this study include the Yonsei University scheme for the planetary boundary layer [*Hong et al*., 2006], the Rapid Radiative Transfer Model longwave scheme [*Mlawer et al*., 1997], the MM5 shortwave scheme [*Dudhia*, 1989] for the shortwave radiation, the Eta surface layer scheme [*Janjic*, 1996, 2002], and a unified Noah land-surface model [*Chen and Dudhia*, 2001].

[10] To investigate the impact of ice hydrometeors on the simulated MCS precipitation, five bulk microphysics schemes are used (listed in Table 1). The WRF single-moment microphysics scheme (WSMMPS) used in this study generally follows *Hong et al*. [2004] and *Hong and Lim* [2006] including ice sedimentation and other new ice-phase parameterizations. The GCE model [*Tao and Simpson*, 1993] one-moment bulk microphysical schemes are mainly based on *Lin et al*. [1983] with additional processes from *Rutledge and Hobbs*. [1983]. These schemes include the 2-ice microphysics scheme with prognostic ice variables of cloud ice and snow (i.e., WSM5 and Goddard 2-ice); 3-ice microphysics schemes with prognostic ice variables of cloud ice, snow, and graupel (i.e., WSM6 and Goddard 3-ice graupel schemes); and Goddard hail scheme which is a three-ice microphysics scheme with prognostic ice variables of cloud ice, snow, and hail.

[11] Despite the variations in different microphysics formulas for the WSMMPS (i.e., WSM5 and WSM6) and the Goddard schemes, the size distributions for rain, snow, and graupel in different schemes are kept consistent (i.e., same intercept and density) among different schemes, in order to reduce the differences between various microphysics schemes caused by these constants. We also find that these

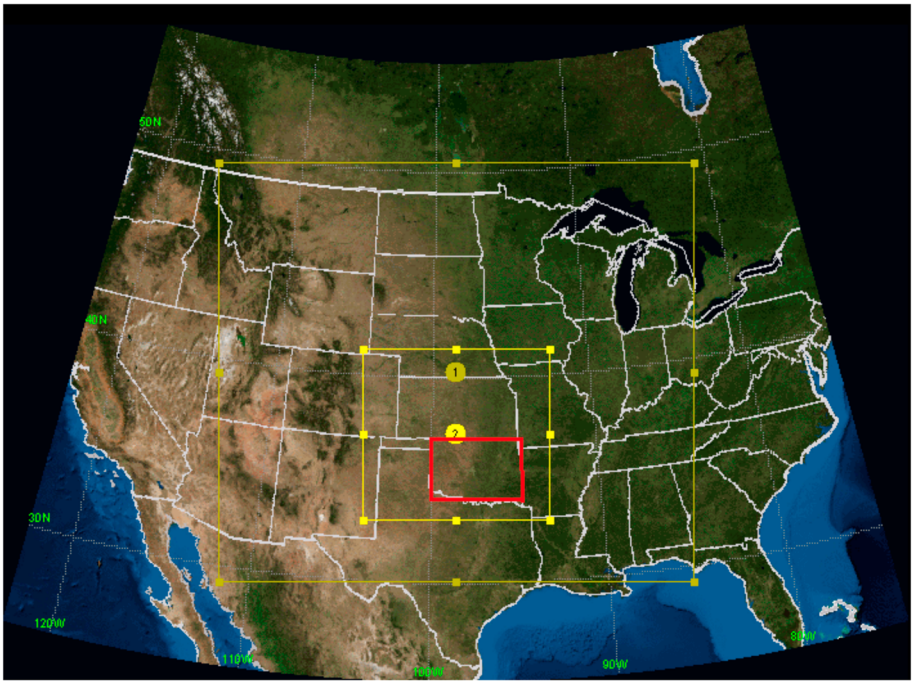

Figure 1. Domains used for the WRF simulations. The outer domain (labeled 1 at the center) has 9 km horizontal resolution. The inner domain (labeled 2) has a horizontal resolution of 3 km and covers the southern plains (Oklahoma and Kansas). The red boundary indicates the area precipitation analysis performed on, which is from 34°N to 37°N and 100°W to 94°W.

constants do not have any significant impact on our results (not shown). The intercepts are 8.0×10^6, 1.6×10^7, 4.0×10^6, and 2.0×10^5 for the rain, snow, graupel, and hail, respectively. The densities are 1000, 100, 300, and 917 kg m^{-3} for the rain, snow, graupel, and hail, respectively. In the original WSM6 and WSM5, the snow intercept parameter is a function of air temperature, following the equation:

$$n_{0S}(m^{-4}) = 2 \times 10^6 \times \cdot\exp[0.12(T_0 - T)] \quad (1)$$

where $T_0 = 273.15$ K. The above formula indicates that the number concentration of snow increases at colder temperatures, which enhances the rate of accretion of ice and sublimation/deposition of snow, and reduces the sedimentation of snow through the reduction of mean size of snow aggregates [*Hong et al.*, 2004]. However, in this study the hydrometeor intercepts in WSM6 and WSM5 are kept as constants.

[12] Rayleigh scattering is assumed for the calculation of radar reflectivity, where the reflectivity factor is the sum of the sixth moment of the hydrometeor size distribution with a dielectric factor applied for ice particles. The parameters used in the calculation are consistent with the previously mentioned particle size distributions. The convective/stratiform partitioning scheme used in this study is based on the horizontal radar reflectivity gradient [*Steiner et al.*, 1995], which is also referred to as a "texture scheme" in the previous literatures. The criteria for identifying the convective region are based on intensity, "peakedness," and the surrounding area as described by *Steiner et al.* [1995]. Several input parameters for the partitioning scheme are tuned [*Feng et al.*, 2011] to fit the midlatitude scenarios because the scheme is originally developed for tropical convection. The 2 km Mean Sea Level (MSL) height is used as the analysis level in order to avoid bright band contamination, and the reflectivity threshold for the convective region is set to 43 dBZ, according to the Z-R relationship in midlatitudes [*Feng et al.*, 2011]. This partitioning scheme is applied to the NEXRAD radar observations and WRF-simulated radar reflectivity such that the model results are evaluated at the same metrics as the observations.

[13] The surface precipitation is also separated into convective and stratiform types by applying the above partitioning scheme. The radar-classified region is superimposed on the Mesonet sites for observations and WRF grid for model simulations. Considering the movement and evolution of the storm, the analysis is performed every 10 min, and then the results are integrated every 2 h period.

4. Results

[14] Two squall line events have been selected over Oklahoma during the periods from 00Z 06 May to 00Z 08 May 2007 (Case 1) and from 00Z 23 May to 00Z 25 May 2007 (Case 2). First, the large-scale synoptic patterns are

Table 1. Microphysics Parameterizations Used for the Sensitivity Study

MP Schemes	**Prognostic Ice Species**
WSM5	cloud ice, snow
Goddard 2-ice (gce2ice)	cloud ice, snow
WSM6	cloud ice, snow, graupel
Goddard 3-ice graupel (gce3ice_gr)	cloud ice, snow, graupel
Goddard hail (hail)	cloud ice, snow, hail

discussed, and then the reflectivity and precipitation fields are compared in detail. Finally, the impacts of various microphysics schemes on WRF simulations are discussed and evaluated against observations.

4.1. Evaluation of the Simulated Squall Line

[15] The 06 May squall line event (Case 1) developed from the remnant convection of a squall line event that occurred on 05 May across Iowa to Oklahoma. The domain of interest (red box in Figure 1) is located to the east of a deep trough with divergence at 03Z 07 May (Figure 2a). The low-level jet transported warm and moist air from the southeast to Kansas and Oklahoma (Figure 2c) providing the favorable support for convective development in the warm sector ahead of the cold front/dry line (Figure 2c). The evidence of a dry line to the west of Kansas and Oklahoma is seen in NARR (Figure 2c) and WRF (Figure 2d), as well as a moist tongue extending to Oklahoma region.

[16] With support from an upper-level trough (Figure 2a) and low-level jet (Figure 2c), the convection matured at 09Z 07 May and developed into a linear MCS. The system moved eastward and dissipated around 00Z 08 May. In the beginning, isolated convective cells formed from a humid and unstable air mass, producing merging outflow boundaries that likely triggered more convection and a widespread and long-lived MCS. The squall line event produced isolated large hail and damaging winds along with heavy rainfall (Storm Prediction Center, 2007). As shown in Figures 3b–3f, WRF did not capture the extended stratiform region as seen from the NEXRAD radar observations (Figure 3a).

[17] All simulations have minor location errors for the orientation of the squall line as compared with the observations. The Goddard 3-ice graupel (Figure 3d) and 2-ice (Figure 3e) schemes have a uniform and continuous structure in radar reflectivity structure in the stratiform region, while the Goddard hail (Figure 3f), WSM6 (Figure 3b), and WSM5 (Figure 3c) schemes have a broken and less continuous feature. The Goddard hail scheme (Figure 3f) displays a narrow and well-defined line formed by convective cells.

[18] The 24 May squall line event (Case 2) occurred under a similar upper-level trough and jet streak location as Case 1 (Figure 2e), providing the lifting mechanism for the event. The model well simulates the wind and pressure patterns at 500 mb (Figure 2f). For the lower level fields (Figure 2g), the temperature and moisture gradients are not as strong as Case 1 (Figure 2c). In general, the model captures the pressure and dew point temperature patterns, but the dew point temperature is much higher than the reanalysis (Figure 2h). This squall line event was associated with less low-level moisture and relatively weaker convection compared to Case 1 (not shown). The system maintained a well-defined linear structure for a longer period than Case 1 (not shown). For all the microphysics schemes, the WRF-simulated reflectivity has better spatial and temporal agreement with NEXRAD observations in Case 2 than in Case 1(Figure 3).

[19] All simulations have a narrower stratiform rain region compared to the radar observations (Figures 3g–3l) at 12Z. As revealed in previous studies, the narrow stratiform coverage is due to the excessive evaporation in single-moment schemes, while the broader stratiform coverage occurs in higher moment bulk schemes and bin microphysics schemes [e.g., *Morrison et al*., 2009; *Luo et al*., 2010; *Li et al*., 2009, 2009a]. Similar to Case 1, both Goddard 3-ice graupel and 2-ice schemes produce horizontal reflectivity structures closer to the observations (i.e., more continuous stratiform region compared to WSM6 and WSM5). The Goddard hail scheme, on the other hand, produces much higher radar reflectivity over the leading convective cells since the Goddard hail scheme was designed for simulating convection with intense updrafts in order to produce hail. Therefore, the hail microphysics scheme produces more reasonable results in Case 1 than in Case 2 where a moderate convective system is observed.

[20] To quantitatively evaluate the simulated precipitation for the two selected cases, Oklahoma Mesonet observations are used in this study. Figure 4 shows the time series of 3 h accumulated precipitation from the Mesonet rain gauge observations and WRF simulations with various 2-ice and 3-ice microphysics schemes (Table 1). For Case 1 (Figure 4a), WSM6 overestimates the total precipitation by 47% compared to the observations, with the peaks shifted ahead by 3 h. The discrepancy is mainly attributed to the overestimation from 03Z to 18Z on 06 May where additional convective cells are simulated over the analysis domain. Total precipitation from Goddard 3-ice graupel and 3-ice hail scheme is the closest to the observations among all the simulations (~10% overestimation). However, both Goddard 3-ice schemes significantly overestimate rainfall during 06 May and underestimate rainfall by ~20% for the peak. The WSM5 and Goddard 2-ice schemes notably underestimate the total precipitation by ~55% and ~73%, respectively. Generally speaking, all simulated peaks occur 3 h ahead of the observations; the magnitudes of the peak produced by 3-ice schemes are similar to the observations, while those simulated from 2-ice schemes are nearly half that of the observations.

[21] For Case 2 (Figure 4b), the simulated precipitation results agree much better than Case 1 in both total precipitation and the magnitudes of the peak. Compared to the observed total precipitation (21 mm), all 3-ice schemes overestimate precipitation by 38% (WSM6), 19% (Goddard 3-ice), and 24% (Goddard 3-ice hail). For both 2-ice schemes, the simulated total precipitation results agree within 14%. All simulated peaks, except for hail, have a 3 h lag behind the observed peaks. The good agreement in this case warrants additional study on the details of the simulated properties including areal coverage and precipitation within the stratiform and convective regions.

4.2. Convective/Stratiform Areal Coverage and Precipitation

[22] To evaluate the WRF-simulated storm structure in the convective and stratiform regions, the *Feng et al*. [2011] classification algorithm has been applied to both radar observations and WRF simulations. The percentages of areal coverage are against the area of the study domain. In comparison to the observed convective areal coverage (2.61%, Figure 5a), all simulations (Figures 5b–5f) overestimate the convective areal coverage ranging from 2.80% for the Goddard 2-ice scheme to 5.21% for WSM6. For the stratiform region (11.65% from NEXRAD), all the 3-ice schemes underestimate the coverage, with the best agreement from gce3ice (11.03%). On the other hand, all the 2-ice schemes have larger stratiform coverage than the observed ones shown in Figure 5, with the best agreement from WSM5 (11.87%).

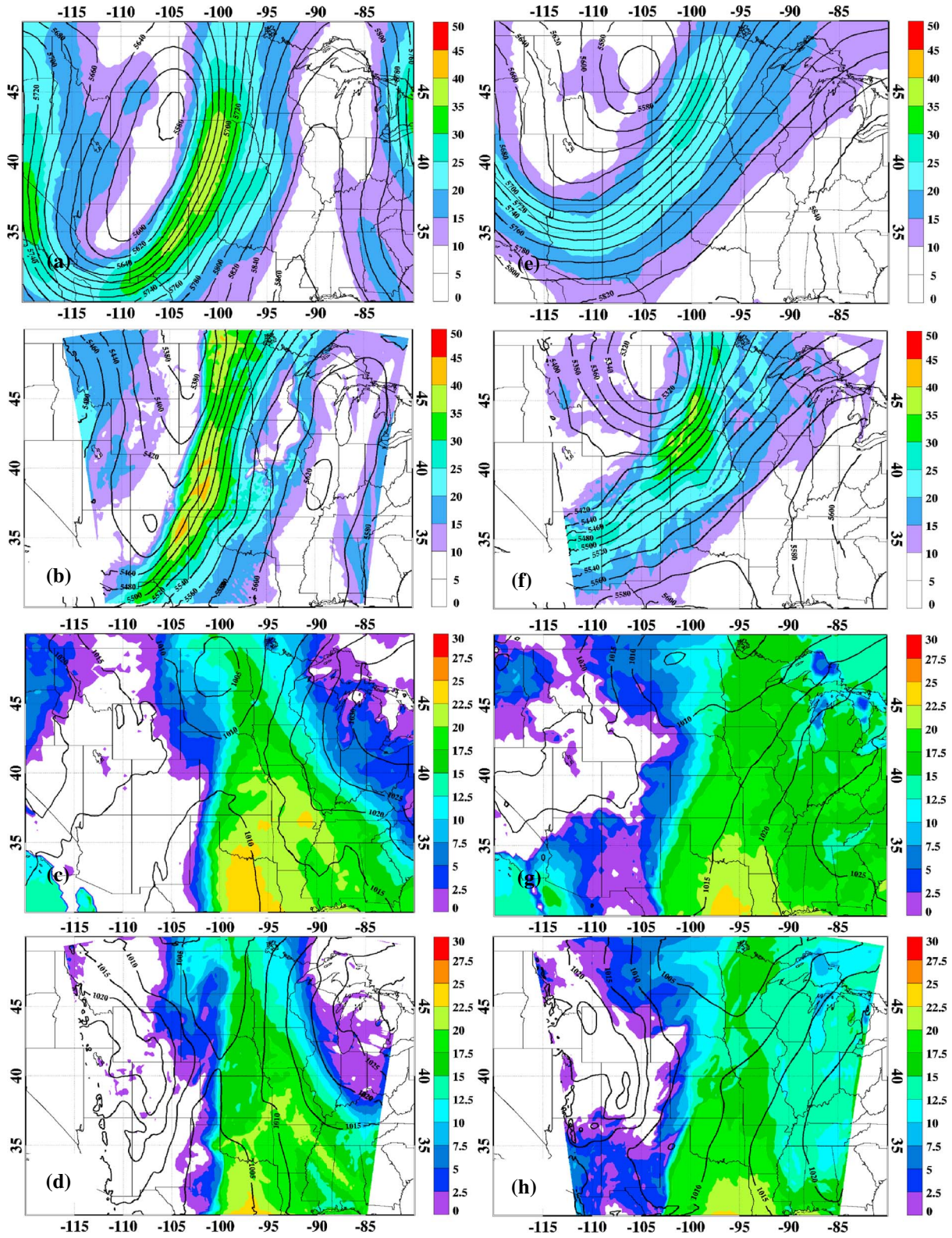

Figure 2. Daily averaged 500 hPa wind magnitude (filled contour) and geopotential height (black contour) from (a) NARR and (b) WRF simulation with WSM6 on 07 May 2007; surface MSLP (black contour), dew point temperature (filled contour) from (c) NARR and (d) WRF at 21Z on 06 May 2007. (e) and (f) Daily average for 23 May 2007; (g) and (h) at 15Z on 23 May 2007. Figures 2e–2h are similar to Figures 2a–2d but for Case 2.

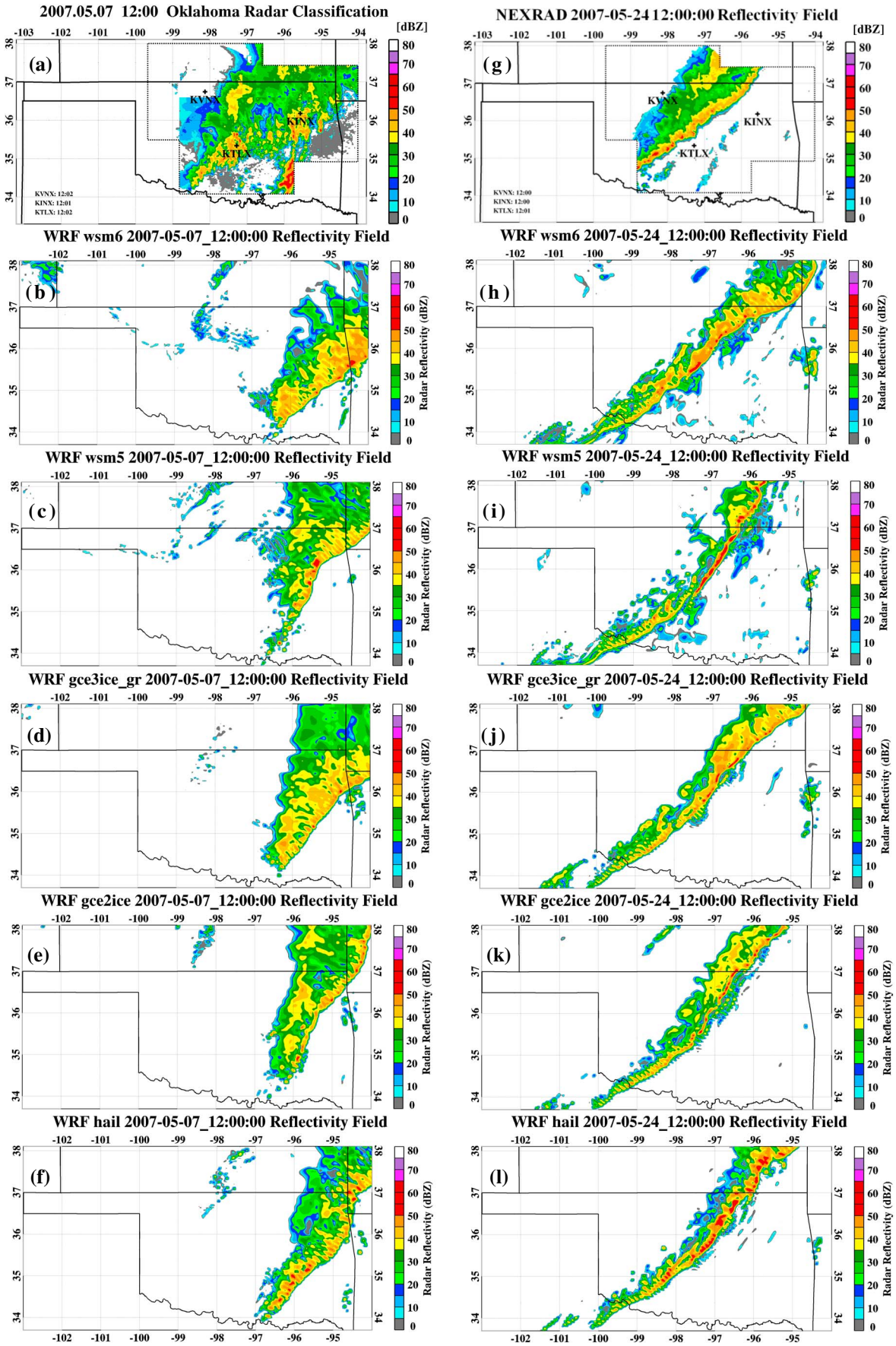
2007.05.07 12:00 Oklahoma Radar Classification
NEXRAD 2007-05-24 12:00:00 Reflectivity Field
WRF wsm6 2007-05-07_12:00:00 Reflectivity Field
WRF wsm6 2007-05-24_12:00:00 Reflectivity Field
WRF wsm5 2007-05-07_12:00:00 Reflectivity Field
WRF wsm5 2007-05-24_12:00:00 Reflectivity Field
WRF gce3ice_gr 2007-05-07_12:00:00 Reflectivity Field
WRF gce3ice_gr 2007-05-24_12:00:00 Reflectivity Field
WRF gce2ice 2007-05-07_12:00:00 Reflectivity Field
WRF gce2ice 2007-05-24_12:00:00 Reflectivity Field
WRF hail 2007-05-07_12:00:00 Reflectivity Field
WRF hail 2007-05-24_12:00:00 Reflectivity Field
(a)
(b)
(c)
(d)
(e)
(f)
(g)
(h)
(i)
(j)
(k)
(l)
KVNX
KINX
KTLX
KVNX: 12:02
KINX: 12:01
KTLX: 12:02
KVNX: 12:00
KINX: 12:00
KTLX: 12:01
[dBZ]
Radar Reflectivity (dBZ)

Figure 3

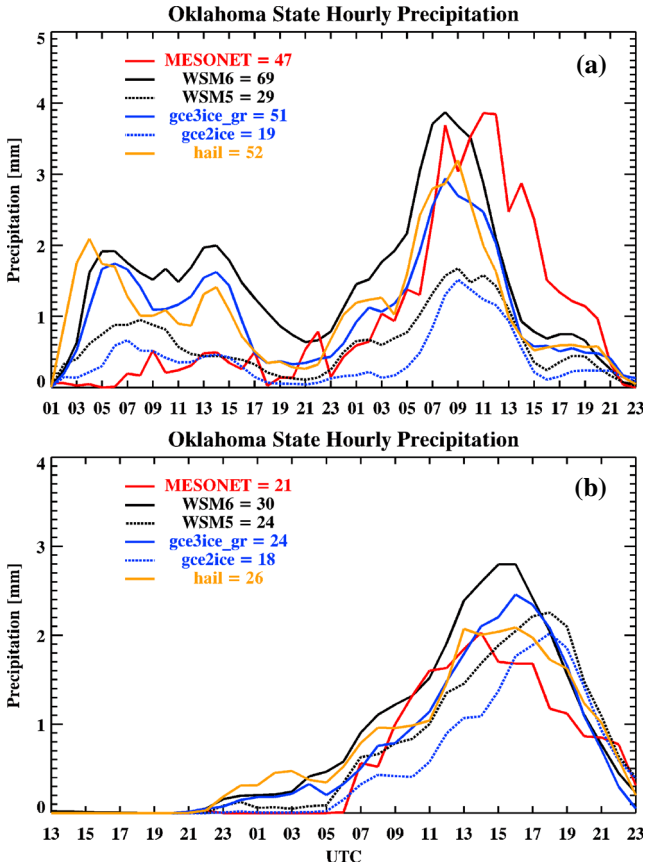

Figure 4. Hourly precipitation from Oklahoma Mesonet observations (red), and WRF simulation from WSM6 (black), WSM5 (blue), WSM6_5 (green), Goddard 3-ice with graupel (dotted black), Goddard 2-ice (dotted blue), and Goddard hail (gold) averaged over the analysis domain (red box in Figure 1). (a) Precipitation from 01Z 06 May to 23Z 07 May 2007, and (b) precipitation from 13Z 23 May to 23Z 24 May 2007. The numbers in the legend represent the total precipitation (in mm).

[23] In order to quantitatively evaluate the simulated precipitation, 2 h of accumulated precipitation is averaged over the convective and stratiform regions from both Mesonet observations and the WRF simulations (Figure 5g–5l). As shown in Figures 5i and 5k, the 2-ice schemes (WSM5 and Goddard 2-ice) underestimate the convective precipitation compared with the observation (15 mm), with the largest differences coming from the Goddard 2-ice scheme (8 mm). On the other hand, the 3-ice schemes (WSM6 and Goddard hail) overestimate the convective precipitation by 4 and 6 mm, respectively. The convective precipitation produced by the Goddard 3-ice graupel scheme (16 mm) is comparable to the observed value. Over the whole period, most schemes overestimate the stratiform precipitation with the exception of the Goddard hail scheme, which produces less rainfall (5 mm) compared with the observations (6 mm). However, all WRF simulations underestimated stratiform rainfall intensity from 6 to 14 UTC.

[24] The differences between the 2-ice and 3-ice schemes are prominent in the convective and stratiform areal coverages. The 2-ice schemes produce less convective areal coverage and more stratiform area coverage than the 3-ice schemes. In other words, by including graupel/hail processes in the simulations, the size of the convective (stratiform) region is increased (decreased). The only notable difference between the Goddard 3-ice graupel and hail schemes is the stratiform coverage during 17 to 20 Z, suggesting that the expanding stratiform region is suppressed in hail scheme. Hail is efficient in accreting small hydrometeor particles and has a higher fall speed than other same-sized hydrometeors. Therefore, more hydrometeors precipitate out in the Goddard 3-ice hail scheme than in other schemes. For example, the Goddard 3-ice hail scheme produces 19% more intensive convective rainfall than the Goddard 3-ice graupel scheme. Thus, there will be fewer hydrometeors left aloft with fewer hydrometeors being able to spread out due to the ascending front-to-rear storm relative flow. Conversely, for the 2-ice scheme, less dense hydrometeors (e.g., particles such as snow with smaller fall velocities) are more likely to be able to spread out to form an extensive stratiform region.

[25] The ratio of convective to stratiform precipitation is a function of hydrometeor composition. If lighter, slow falling ice-phased particles (i.e., snow) are present in clouds, the ratio of convective to stratiform precipitation tends to be smaller, and therefore the model-simulated ratios are much lower than observations. Conversely, if heavier, fast falling ice-phased particles are present in clouds, the simulated ratios are higher than the observations. Overall, the Goddard 3-ice graupel (2.0) and WSM6 (2.9) simulated ratios are closer to the observation (2.3).

4.3. Vertical Distribution of Squall Line Structures

[26] Figure 6 shows a snapshot of the horizontal radar reflectivity field, the horizontally classified DCS components based on radar reflectivity [*Feng et al.*, 2011], and vertical cross sections of the radar reflectivity observed by the KTLX radar (Figure 6a) and simulated by the WRF model (Figure 6b–6f) on 24 May. As illustrated in Figure 6, the simulated radar reflectivities and classified components qualitatively agree well with radar observations. The 5–10 dBZ echo tops are similar with values around 12–13 km. The simulated 40–50 dBZ echo extends higher (~ 10 km) than the observations (~ 6 km). That said reflectivity in the convective region has large variability in the simulations compared to observations, especially above 6 km.. Multicellular features are also evident in the WRF simulations as opposed to a horizontally homogeneous stratiform region in the observations. These multicellular features are commonly observed in bulk microphysics schemes [*Li et al.*, 2009a, 2009b].

[27] For WRF simulations (Figure 6b–6f), the strongest updrafts occur within the classified convective regions. To reveal the bulk vertical wind characteristics in the simulated 3-D

Figure 3. Comparison of radar observed and model-simulated reflectivity at 1 km AGL from (a), (g) NEXRAD radar, (b), (h) simulations from WRF WSM6, (c), (i) WSM5, (d), (j) Goddard 3-ice graupel, (e), (k) Goddard 2-ice, and (f), (l) Goddard hail. Figures 3a–3f are for Case 1 on 07 May 2007; Figures 3g–3l are for Case 2 on 24 May 2007.

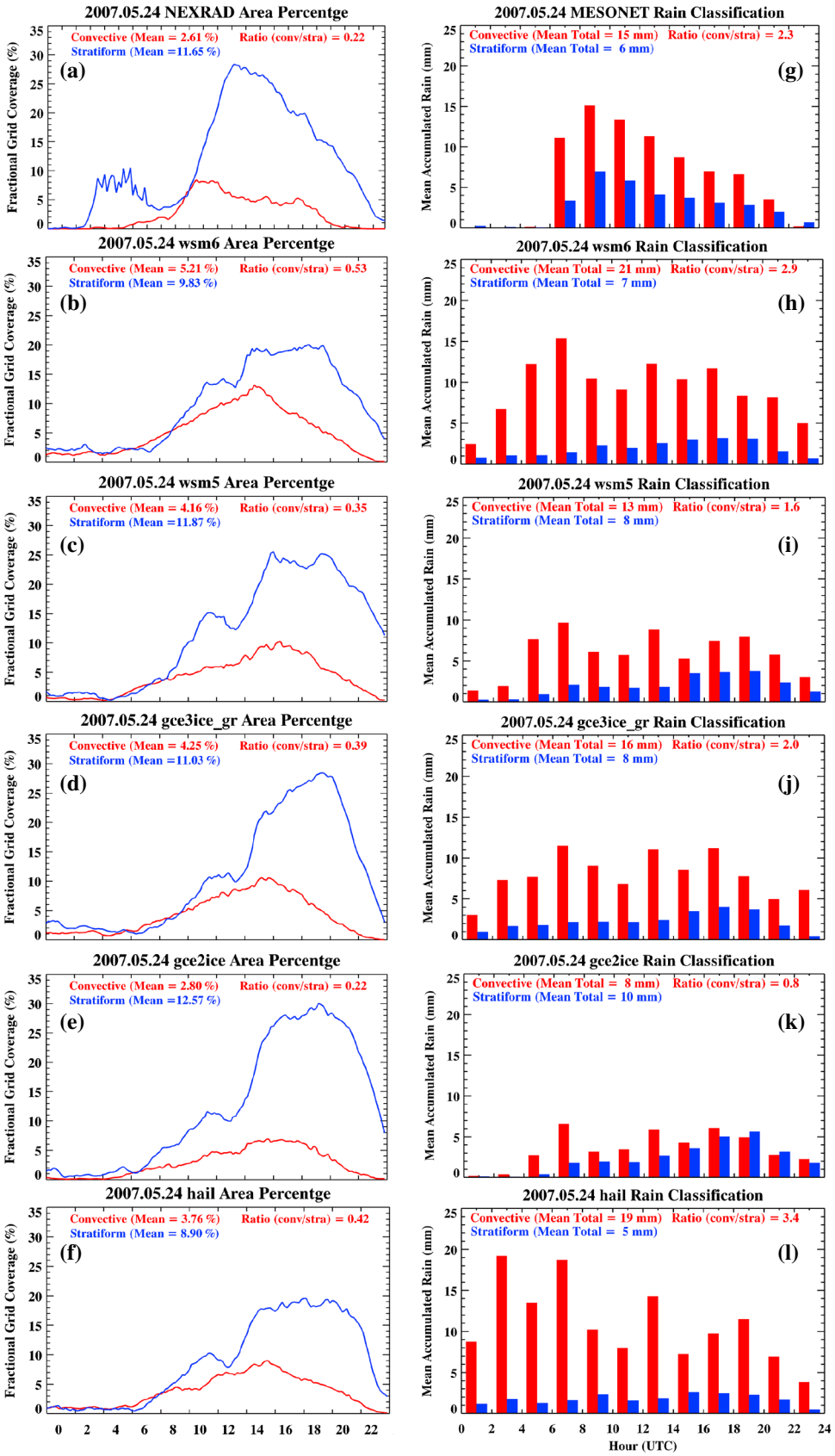

Figure 5. (left column) Area coverage and (right column) precipitation rate in every 2 h for convective (red) and stratiform (blue) regions from (a) observations from NEXRAD and (g) Mesonet, (b) (h) WSM6, (c) (i) WSM5, (d) (j) Goddard 3-ice with graupel, (e) (k) Goddard 2-ice, and (f) (l) Goddard 3-ice with hail.

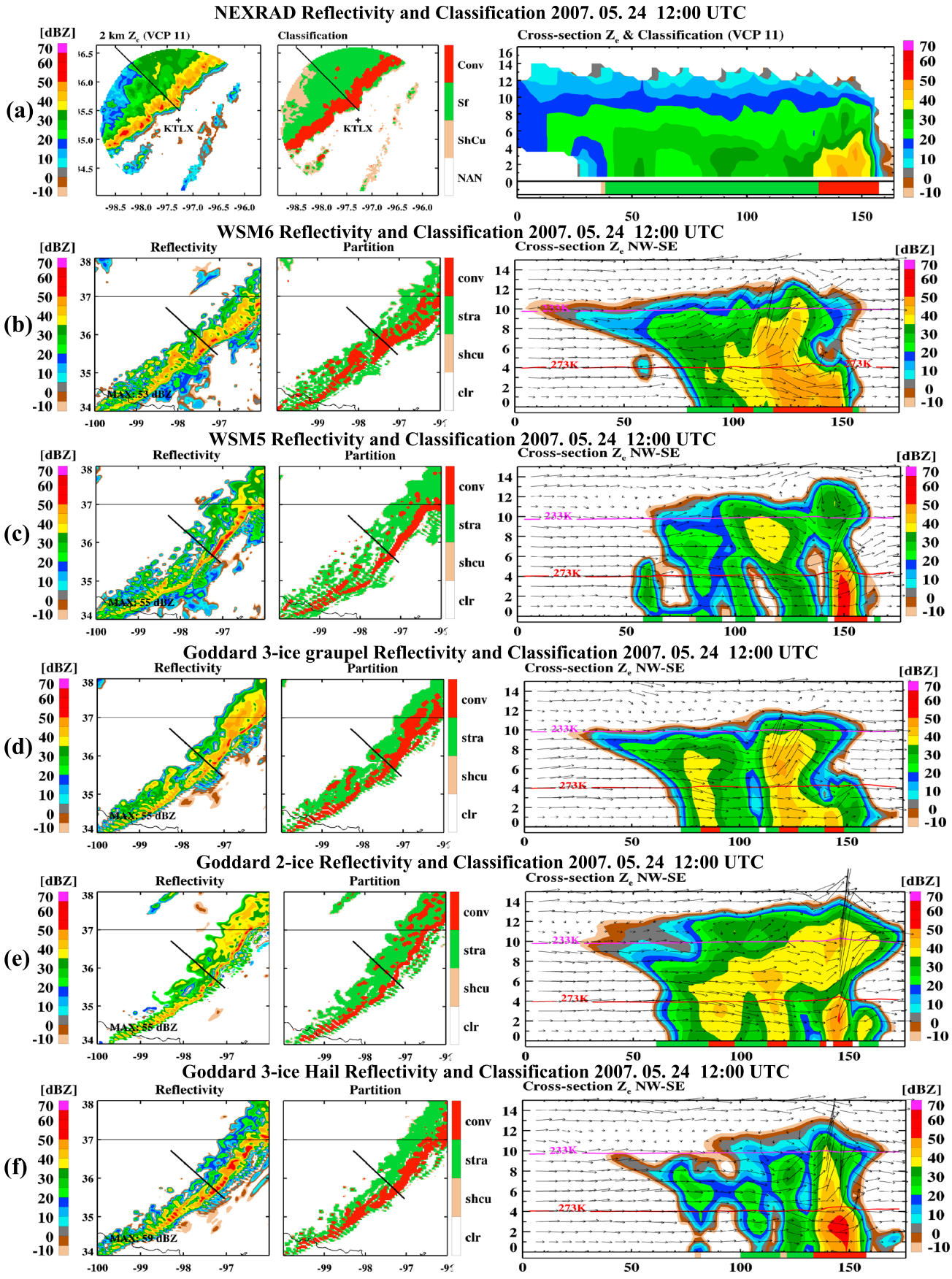
NEXRAD Reflectivity and Classification 2007. 05. 24 12:00 UTC
(a)
2 km Ze (VCP 11)
Classification
Cross-section Ze & Classification (VCP 11)
KTLX
Conv
Sf
ShCu
NAN
WSM6 Reflectivity and Classification 2007. 05. 24 12:00 UTC
(b)
Reflectivity
Partition
Cross-section Ze NW-SE
conv
stra
shcu
clr
MAX: 53 dBZ
233K
273K
WSM5 Reflectivity and Classification 2007. 05. 24 12:00 UTC
(c)
MAX: 55 dBZ
Goddard 3-ice graupel Reflectivity and Classification 2007. 05. 24 12:00 UTC
(d)
Goddard 2-ice Reflectivity and Classification 2007. 05. 24 12:00 UTC
(e)
Goddard 3-ice Hail Reflectivity and Classification 2007. 05. 24 12:00 UTC
(f)
MAX: 59 dBZ
[dBZ]

Figure 6

volume data, Contoured-Frequency-with-Altitude Diagrams (CFADs) [e.g., *Yuter and Houze*, 1995; *Steiner et al*., 1995; *Lang et al*., 2003] of vertical velocity are generated for both the convective and stratiform regions (Figure 7). The CFADs are produced from the simulations at 10 min intervals from 00 UTC to 24 UTC on 24 May 2007. The CFAD bin size is 1 m/s with a range of −15 to 50 m/s. As demonstrated in Figure 7, the updrafts in the convective region are much stronger than those in the stratiform region in all simulations, indicating that the reflectivity-based partitioning scheme can reasonably separate the dynamical wind fields. Although there are still some high vertical velocity values in stratiform region, which are probably due to the tilting of convective updrafts, this feature only takes less than 0.1% of the grid and does not have a main impact on statistics. The convective updrafts in all 3-ice schemes are stronger than those in the 2-ice schemes, especially at upper levels (10 km), presumably due to more concentrated latent heat released from riming in the 3-ice schemes. Despite the obvious differences between the 2-ice and 3-ice schemes in the convective updraft, the differences are not obvious in the stratiform region. In addition, the Goddard hail scheme produces very weak vertical wind in the stratiform region.

[28] The CFADs of reflectivity are generated in Figure 8 from both NEXRAD radar and WRF for the convective and stratiform regions. The CFADs are produced from the reflectivity volume at 10 min intervals from 08 to 18 UTC on 24 May 2007 as the squall line is fully developed and well contained in the analysis domain during this time period. The CFAD bin size is 1 dBZ ranging from 5 to 60 dBZ. There are obvious differences in the reflectivity distribution characteristics between simulations and observations.

[29] At the lower levels of the convective region, the frequency maxima for the 3-ice schemes are located around 40–45 dBZ, which are slightly higher than the observations. The frequency maxima for the 2-ice schemes are located around 40 dBZ, due to lighter precipitation (Figure 5) in the 2-ice compared with 3-ice schemes. For middle to upper levels (> 4 km in altitude) of the convective region (Figures 8a–8f), the frequency maxima in observations lean toward smaller values due to a reduced number of large particles. At the level of ~6 km, the observed frequency maxima are located at ~30 dBZ, which is less than those below 4 km (~40 dBZ). In contrast, most simulations have frequency maxima that are ~40 dBZ at 6 km (except for the hail scheme) and are almost constant from the surface up to 6 km. Also of note in the vertical cross sections (Figures 6c, 6e) is an increased reflectivity region (right above the convective core) for the 2-ice schemes. This may be due to the lack of fast falling ice species (i.e., graupel or hail).

[30] In order to investigate the simulated reflectivity biases in reflectivity distribution spectrums, the 10th, 50th, 90th, and 99th percentile of reflectivity for observations and simulations are plotted in Figure 9. For example, the 10th percentile line (Figure 9a) represents those grids with reflectivity values in the bottom 10% of the distribution spectrum. As discussed previously, the simulations in both convective and stratiform regions lack the approximately linear decrease in maximum reflectivity values from ~4 km to echo top. In the convective region, the largest discrepancy between models and observations occurs above 4 km (Figures 9a–9d). For the 50th percentile, which is the median of the reflectivity distribution, 3-ice schemes generally have higher (lower) reflectivity values than 2-ice schemes below 6 (above 8) km. The 10th percentile also displays this characteristic (Figures 9a and 9b). For the 90th and 99th percentiles (top 10% and 1% of the distribution spectrum), differences between model and observations generally increase with height; 3-ice schemes have higher reflectivity values than the 2-ice schemes at the midlevel to upper level.

[31] Discrepancies between the model and observations also occur in the stratiform region. For example, between 6 and 8 km, most observed radar reflectivities are less than 25 dBZ, while the simulated frequency maxima are around 25–40 dBZ (Figure 8), and this feature is also evident in the 50th percentile profiles (Figure 9f). Two ice schemes have higher reflectivities in the stratiform region compared to their counterpart 3-ice schemes at most levels (Figures 9e–9g). At most grid points, WSM6 has the best resemblance with observations in the stratiform region. In rare occasions (in the 99th percentile), the simulated maximum reflectivities (except for hail scheme) exceed 40 dBZ above 6 km (Figures 8 and 9h). Since the convective/stratiform partition scheme only considers the reflectivity at 2 km, the upper level of a tilted convective core could be counted as stratiform, causing these very high reflectivity values in stratiform regions. Hail scheme, despite having a positive bias at ~8 km, has a lower reflectivity above 10 km in both convective and stratiform regions. In general, 3-ice schemes produce more high reflectivity values in convective regions, while 2-ice schemes produce more high reflectivity values in stratiform regions.

[32] Figure 10 shows the time and domain-averaged vertical profile of hydrometeor mixing ratios. There is more snow and cloud ice distributed in the stratiform region than in the convective region for all simulations. In addition, less graupel and hail are seen in the stratiform region than in the convective region in the 3-ice scheme. These features are consistent with reasonable separation of convective and stratiform regions. Compared to WSMMPS (i.e., WSM5 and WSM6), the Goddard schemes (i.e., 2-ice and 3-ice graupel) tend to produce even higher reflectivity values in the midlevels (6–8 km) for both the convective and stratiform regions. As shown in Figure 10, Goddard schemes produce larger mean snow and graupel mixing ratio than their 2-ice or 3-ice counterparts in WSMMPS. At the same time, the area differences between Goddard scheme and WSM schemes are very limited, which is less than 2% of the whole domain (Figure 5). This shows that the larger mean snow and graupel mixing ratio in Goddard scheme is attributed to more snow and graupel condensate in Goddard schemes. In the WRF model, the advection scheme treats all the hydrometeors as a bulk quantity. Thus, higher amounts of

Figure 6. (left) Radar reflectivity at 1 km AGL, (middle) classified DCS components based on radar reflectivity, and (right) vertical cross section radar reflectivity, with the classification color-coded underneath. Cross-section line shows in radar reflectivity and partition plot. (a) NEXRAD, (b) WRF simulation from WSM6, (c) WSM5, (d) Goddard 3-ice graupel, (e) Goddard 2-ice, (f) Goddard 3-ice hail scheme.

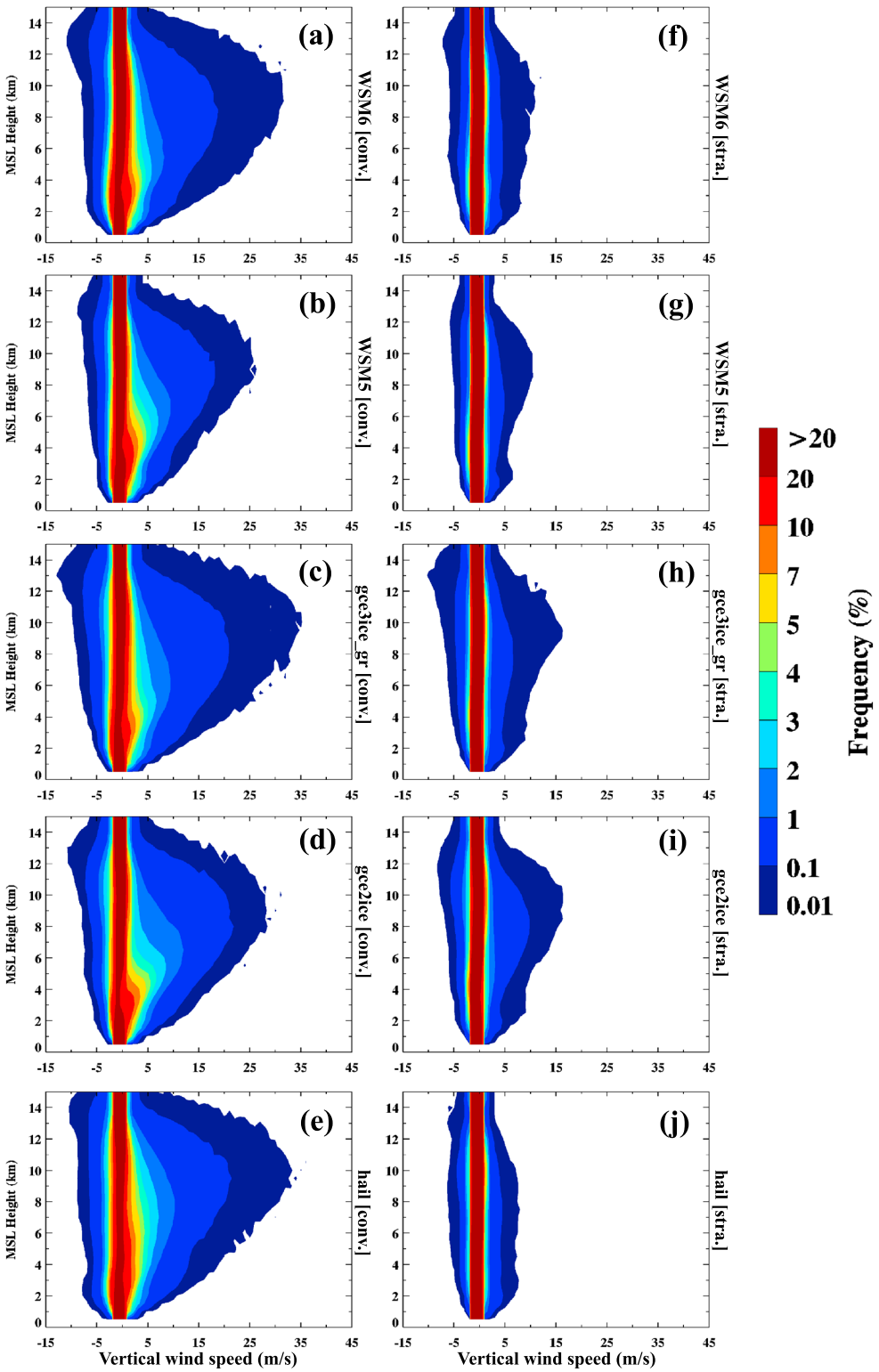

Figure 7. Contoured-Frequency-with-Altitude Diagrams (CFADs) for vertical wind speed over (left column) convective region and (right column) stratiform region for (a), (f) WSM6, (b), (g) WSM5, (c), (h) Goddard 3-ice graupel, (d), (i) Goddard 2-ice, (e), (j) Goddard 3-ice hail.

hydrometeors in the clouds means more hydrometeors can be transported and advected to a larger region. This can explain how the Goddard 2-ice scheme (Figures 5e and 6e) produces a much wider stratiform region than WSM5 (Figures 5c and 6c). Within this process, a dominant variable is the fall velocity of hydrometeor species. Because of the slower fall speed of snow compared with graupel, more ice particles are left aloft in the 2-ice simulations (e.g., reflectivity increase in

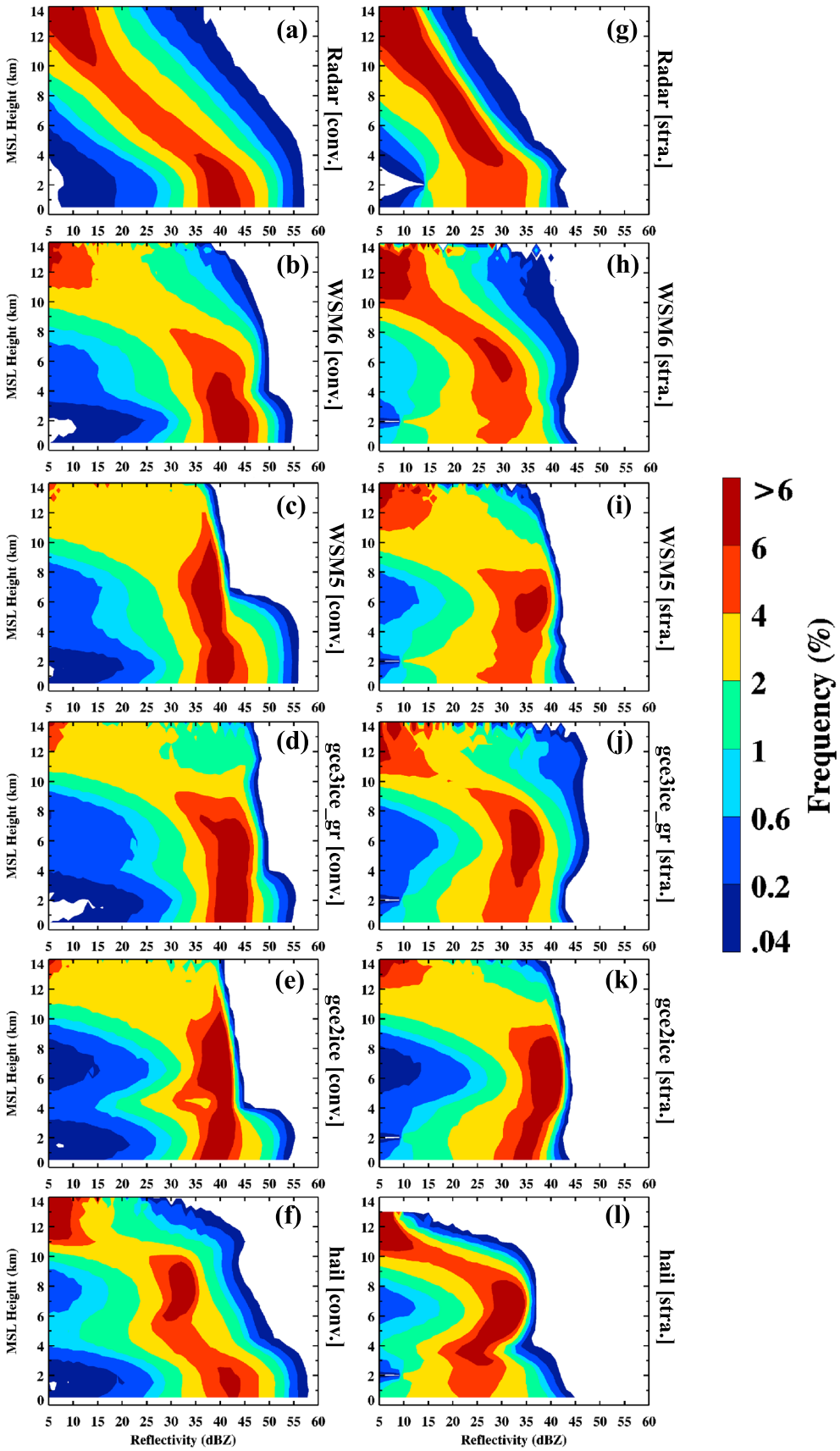

Figure 8. Reflectivity CFADs over (left column) convective region and (right column) stratiform region for (a), (g) NEXRAD radar, (b), (h) WSM6, (c), (i) WSM5, (d), (j) Goddard 3-ice graupel, (e), (k) Goddard 2-ice, (f), (l) Goddard 3-ice hail.

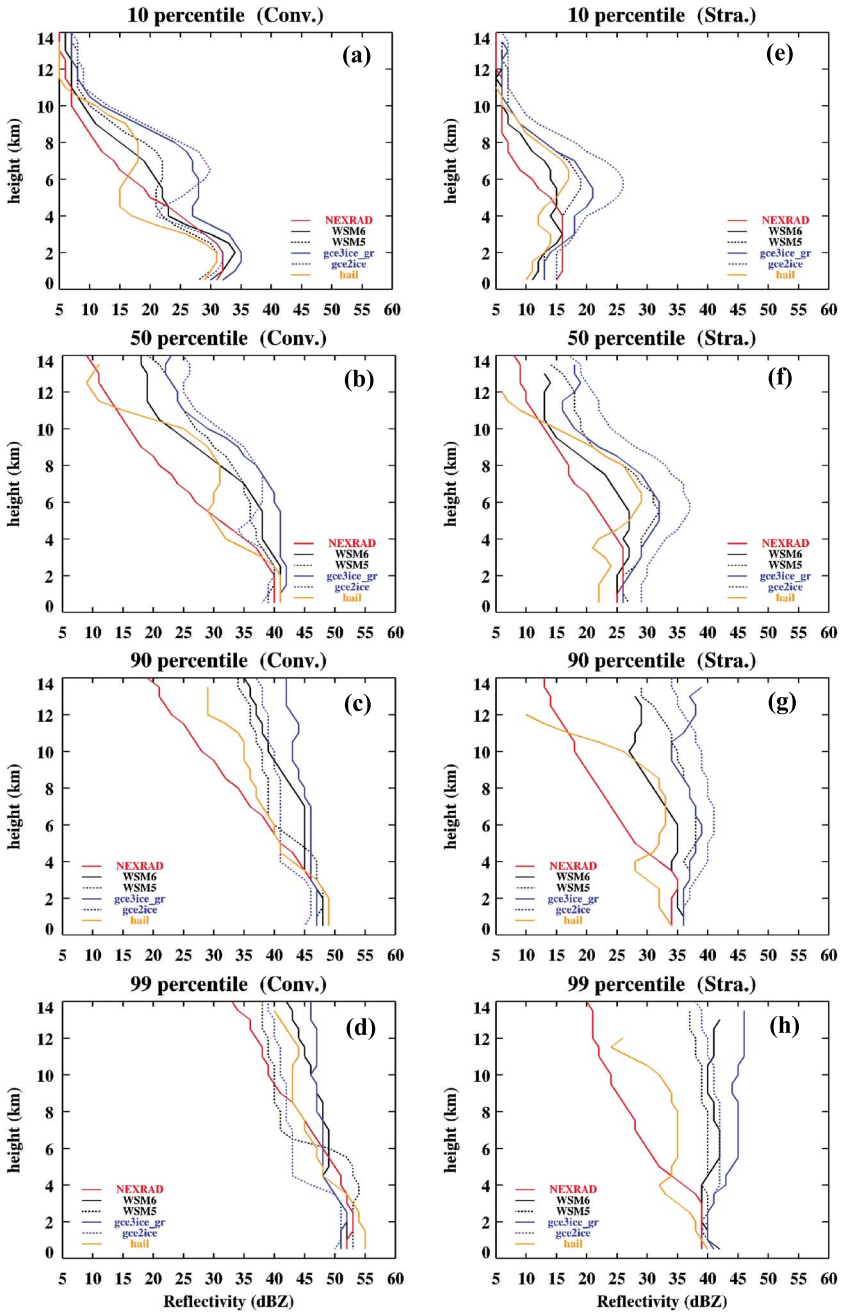

Figure 9. Vertical profile of 10th, 50th, 90th, and 99th percentiles of reflectivity frequency over (a)–(d) convective region and (e)–(h) stratiform region.

10 km in Figure 6e) than in the 3-ice simulations. As a result, there is an obvious decrease in reflectivity field of the convective region in Goddard 3-ice hail (Figure 8f) than Goddard 3-ice graupel (Figure 8d) due to hail having a faster fall speed than graupel.

[33] Despite the models reproducing general structures of the squall line at the lower level, many problems remain as shown in the CFAD plot, such as higher reflectivity values aloft in both convective and stratiform regions. Quite often, the discrepancies between model output and observations exist in the midlevel to upper level (above 6 km), which results from the inability of the model to accurately represent the particle size distribution, ice processes, and storm dynamics.

[34] Considering the microphysics processes alone, there are some apparent problems in the current single-moment schemes: hail processes that facilitate and produce the most precipitation. Thus, in the hail scheme, there are more convective hydrometeors aloft with fewer in-cloud hydrometeors overall. As a result, a smaller stratiform region will form because of overall reduced hydrometeors aloft, and with fewer hydrometeors aloft, the stratiform radar reflectivity value will be lower at midlevels. Recent studies show that the stratiform rain regions in convective systems have important roles in the organization and lifetime of convective systems [*Del Genio et al.*, 2012; *Feng et al.*, 2012]. Therefore, unrealistic stratiform rain structures may result in incorrect

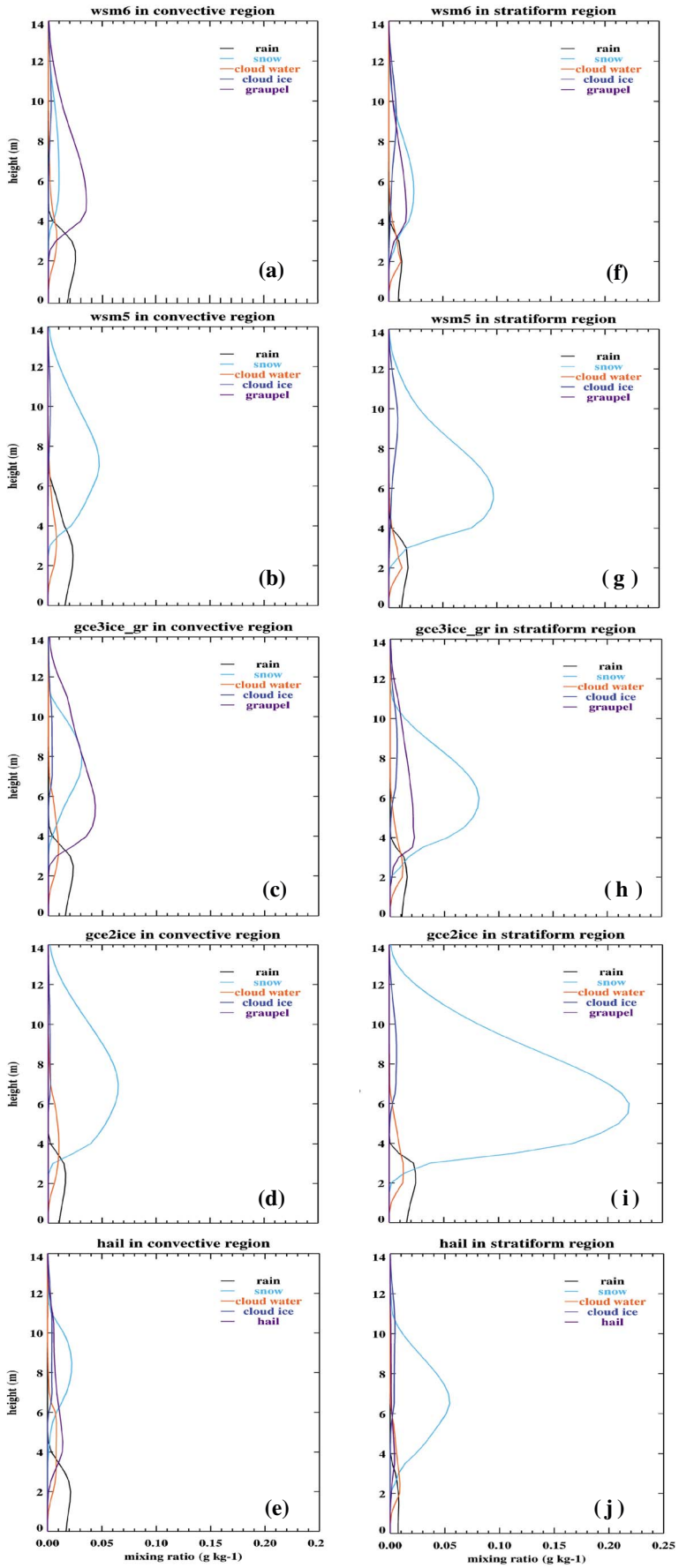
wsm6 in convective region
wsm6 in stratiform region
wsm5 in convective region
wsm5 in stratiform region
gce3ice_gr in convective region
gce3ice_gr in stratiform region
gce2ice in convective region
gce2ice in stratiform region
hail in convective region
hail in stratiform region
rain
snow
cloud water
cloud ice
graupel
hail
height (m)
mixing ratio (g kg-1)
(a)
(b)
(c)
(d)
(e)
(f)
(g)
(h)
(i)
(j)

Figure 10

representation of convective processes. On the other hand, 2-ice schemes lack both graupel and hail processes, which means more lighter particles, slower fall speeds, and less effective precipitation production as compared to 3-ice schemes. Less precipitation coupled with slower hydrometeor fall speeds aloft typically leads to an extended trailing stratiform region. The 3-ice schemes with graupel/hail processes have resolved some problems, such as increased precipitation and reduced midlevel snow accumulation. In order to achieve an optimum and balanced result, ice processes may need to be reexamined, such as accretion and/or conversion rate of snow, graupel, and hail processes [*Lang et al*., 2007, 2011]. Furthermore, more detailed microphysics schemes, such as higher moment schemes or 4-ice schemes (i.e., cloud ice, snow, graupel, and hail) may be needed to properly represent these evaluated features.

5. Conclusions

[35] In this study, two squall line events are studied over the Oklahoma-Kansas region on 6–7 and 23–24 May 2007 using observations and WRF simulations. Both cases are simulated in WRF using 2-ice and 3-ice microphysics schemes and then compared with the surface NEXRAD and Oklahoma Mesonet observations. The reflectivity-based convective/stratiform classification algorithm [*Steiner et al*., 1995; *Feng et al*., 2011] is applied to both the simulated and observed data sets in order to identify the areal converge, precipitation, and vertical structure of these two separated regions. The differences between the 2-ice and 3-ice microphysics schemes are investigated in order to understand the impact of graupel/hail processes on simulated precipitation. Based on an integrative analysis of simulations and observations, the following results are found:

[36] 1. For horizontal radar reflectivity distributions, the Goddard 2-ice and 3-ice graupel schemes produce a continuous uniform structure for the stratiform region, while the Goddard hail, WSM6, and WSM5 schemes display a broken and less uniform area. For both cases, all 3-ice schemes overestimate the total precipitation with the largest overestimation being from WSM6. Both 2-ice schemes produce less total precipitation than the 3-ice schemes.

[37] 2. When comparing the partitioned areal coverage and precipitation over the convective and stratiform regions, all simulations overestimate the convective areal coverage compared with the observations. By including the graupel/hail processes, the areal coverage and precipitation intensity increase in the convective region and decrease in the stratiform region. On the other hand, the 2-ice schemes that do not have any dense precipitating ice species with relatively high vertical fall velocities, such as graupel or hail, are more likely to spread out to form an extensive stratiform region.

[38] 3. As demonstrated in the CFAD plots, the vertical distribution of reflectivity is sensitive to the selection of schemes and the choices of snow, graupel, and hail categories. The model simulations have higher reflectivity compared with the observations, with the largest discrepancy $\geq$ 6 km. In convective regions, 3-ice schemes have higher reflectivity than 2-ice schemes at $<$ 6 km, while 2-ice schemes have higher reflectivity values than 3-ice schemes at heights $>$ 8 km for the 50th and 10th percentiles. In the 90th and 99th percentiles, 3-ice schemes produce higher reflectivity than 2-ice schemes in the midlevel to upper level. In stratiform regions, 2-ice schemes have higher reflectivity than their counterpart 3-ice schemes at most levels for the 10th, 50th, and 90th percentiles. And WSM6 has the closest resemblance to the observations in the stratiform region. In general, 3-ice schemes produce more high reflectivity values in convective regions, while 2-ice schemes produce more high reflectivity values in stratiform regions.

[39] 4. Both 2-ice schemes (i.e., WSM5 and Goddard 2-ice) tend to produce weak convective precipitation and high vertical radar reflectivity aloft, due to the lack of graupel processes. The 3-ice schemes, on the other hand, overestimate convective areal coverage and precipitation, while the overall vertical radar reflectivity structures are more realistic than the 2-ice schemes. This study shows that each bulk scheme evaluated in this study has its advantages and shortcomings. For example, the hail scheme facilitates precipitation formation, resulting in more convective precipitation, less total hydrometeors aloft, and lower radar reflectivity at midlevels. On the other hand, a smaller stratiform region is formed because of less hydrometeors left aloft. The 2-ice schemes do not produce precipitation as effectively as the other schemes due to the lack of either graupel or hail processes. With less precipitation, more hydrometeors remain aloft and higher radar reflectivity occurs at the midlevels, which produces a relatively more homogeneous and extended stratiform region.

[40] 5. This study has also investigated the application of a radar-reflectivity-based convective/stratiform partitioning algorithm [*Steiner et al*., 1995; *Feng et al*., 2011] in WRF simulations. The results demonstrate that the algorithm is able to identify both convective and stratiform regions reasonably in the following aspects: convective precipitation is heavier than stratiform precipitation (Figure 5g–5l); strong updrafts occur more often in the convective region than in the stratiform region (Figure 7); and snow and cloud ice resides largely in stratiform region, while graupel and hail resides largely in convective region (Figure 9). Detailed observations of in-storm wind and microphysics will be needed for quantitative validations in the future work.

[41] In summary, graupel/hail processes appear to play an important role in determining the storm structure. Further investigation can be conducted on more cases, especially for those with heavier stratiform precipitation and in weakly forced environments. All 2-ice schemes are unable to capture the observed structure of a squall line. By including the graupel/hail processes (Goddard 3-ice graupel/hail and WSM6), the 3-ice schemes are able to improve the convective and stratiform features in the squall lines. However, the improvements are limited. This suggests that while the basic structure can be captured by 3-ice schemes, 4-ice schemes may be needed to properly represent these evaluated features. In addition, the study shows the limitations of single-moment bulk

Figure 10. The time-averaged and domain-averaged hydrometeor mixing ratio vertical profiles for the convective region (a–e) and stratiform region (f–j) for WSM6 (a) (f), WSM5 (b) (g), Goddard 3-ice graupel (c) (h), Goddard 2-ice (d) (i), Goddard 3-ice hail (e) (j).

schemes, which is possibly induced by the crude assumptions of hydrometeor size distributions that can introduce significant amount of errors in model simulations. Thus, spectra-bin schemes should be considered in future microphysics validations. Detailed observations for in-storm 3-D winds and microphysics for quantitative validations of the model microphysics schemes and simulations will be needed from field campaigns, such as MC3E (Midlatitude Continental Convective Clouds Experiment). The differences between the simulations and observations are not only contributed from the uncertainties in microphysics schemes, initial condition (i.e., NARR), and other physical processes (e.g., cumulus, land-surface, or radiation schemes) also contribute to the forecast errors; however, they are beyond the scope of this study.

[42] **Acknowledgments.** Surface data and Oklahoma Mesonet precipitation were obtained from the Atmospheric Radiation Measurement Program sponsored by the U.S. Department of Energy Office of Energy Research, Office of Health and Environmental Research, Environmental Sciences Division. We are in debt to Song-You Hong from Yonsei University for providing reflectivity calculation algorithm based on WSM6 scheme. Comments from three anonymous reviewers improved the manuscript and are appreciated. We are also very grateful to Samson Hagos at PNNL for his constructive comments. This research was primarily supported by NOAA GOES-R project managed by Ingrid Guch and Mark DeMaria with award NA11NES440004 at the University of North Dakota. The University of North Dakota authors were also supported by DOE ASR project with award number DE-SC0008468, and NASA EPSCoR CAN under grant NNX11AM15A. The PNNL author is also supported by the DOE Atmospheric System Research (ASR) program.

References

Brock, F. V., K. C. Crawford, R. L. Elliott, G. W. Cuperus, S. J. Stadler, H. L. Johnson, and M. D. Eilts (1995), The Oklahoma Mesonet: A technical overview, *J. Atmos. Oceanic Technol.*, *12*, 5–19.

Chen, F., and J. Dudhia (2001), Coupling an advanced land-surface/hydrology model with the Penn State/ NCAR MM5 modeling system. Part I: Model description and implementation, *Mon. Weather Rev.*, *129*, 569–585.

Churchill, D. D., and R. A. Houze (1984), Development and structure of winter monsoon cloud clusters on 10 December 1978, *J. Atmos. Sci.*, *41*, 933–960.

Cotton, W. R., M. A. Stephens, T. Nehrhorn, and G. J. Tripoli (1982), The Colorado State University three-dimensional cloud/mesoscale model-1982. Part II: An ice phase parameterization, *J. Rech. Atmos.*, *16*, 295–320.

Del Genio, A. D., J. Wu, and Y. Chen (2012), Characteristics of mesoscale organization in WRF simulations of convection during TWP-ICE, *J. Climate*, *25*(17), 5666–5688.

Dudhia, J. (1989), Numerical study of convection observed during the winter monsoon experiment using a mesoscale two-dimensional model, *J. Atmos. Sci.*, *46*, 3077–3107.

Feng, Z., X. Dong, B. Xi, C. Schumacher, P. Minnis, and M. Khaiyer (2011), Top-of-atmosphere radiation budget of convective core/stratiform rain and anvil clouds from deep convective systems, *J. Geophys. Res.*, *116*, D23202, doi:10.1029/2011JD016451.

Feng, Z., X. Dong, B. Xi, S. McFarlane, A. Kennedy, B. Lin, and P. Minnis (2012), Life cycle of midlatitude deep convective systems in a Lagrangian framework, *J. Geophys. Res.*, *117*, D23201, doi:10.1029/2012JD018362.

Ferrier, B. S., W.-K. Tao, and J. Simpson (1995), A double-moment multiple-phase four-class bulk ice scheme. Part II: Simulations of convective storms in different large-scale environments and comparisons with other bulk parameterizations, *J. Atmos. Sci.*, *52*, 1001–1033.

Fovell, R. G., and Y. Ogura (1988), Numerical simulation of a midlatitude squall line in two dimensions, *J. Atmos. Sci.*, *45*, 3846–3879.

Gilmore, M. S., J. M. Straka, and E. N. Rasmussen (2004a), Precipitation evolution sensitivity in simulated deep convective storms: Comparisons between liquid-only and simple ice and liquid phase microphysics, *Mon. Weather Rev.*, *132*, 1897–1916.

Gilmore, M. S., J. M. Straka, and E. N. Rasmusse (2004b), Precipitation and evolution sensitivity in simulated deep convective storms: Comparisons between liquid-only and simple ice and liquid phase microphysics, *Mon. Weather Rev.*, *132*, 1897–1916.

Hong, S.-Y., and J.-O. J. Lim (2006), The WRF single-moment 6-class microphysics scheme (WSM6), *J. Korean Meteorol. Soc.*, *42*, 129–151.

Hong, S.-Y., J. Dudhia, and S.-H. Chen (2004), A revised approach to ice microphysical processes for the bulk parameterization of clouds and precipitation, *Mon. Weather Rev.*, *132*, 103–120.

Hong, S.-Y., Y. Noh, and J. Dudhia (2006), A new vertical diffusion package with an explicit treatment of entrainment processes, *Mon. Weather Rev.*, *134*, 2318–2341.

Houze, R. A. (1973), A climatological study of vertical transports by cumulus-scale convection, *J. Atmos. Sci.*, *30*, 1112–1123.

Houze, R. A. (1977), Structure and dynamics of a tropical squall-line system observed during GATE, *Mon. Weather Rev.*, *105*, 1540–1567.

Houze, R. A., Jr. (1982), Cloud clusters and large-scale vertical motions in the tropics, *J. Meteorol. Soc. Jpn.*, *60*, 396–410.

Houze, R. A., Jr. (2004), Mesoscale convective systems, *Rev. Geophys.*, *42*, RG4003, doi:10.1029/2004RG000150.

Houze, R. A., S. Brodzik, C. Schumacher, S. E. Yuter, and C. R. Williams (2004), Uncertainties in Oceanic Radar rain maps at Kwajalein and implications for satellite validation, *J. Appl. Meteor.*, *43*, 1114–1132.

Janjic, Z. I. (1996), The surface layer in the NCEP Eta Model, Paper presented at 11th Conference on Numerical Weather Prediction, Norfolk, VA, Amer. Meteor. Soc., Boston, MA, 354–355.

Janjic, Z. I. (2002), Nonsingular implementation of the Mellor–Yamada Level 2.5 Scheme in the NCEP Meso model, *NCEP Office Note, 437*, 61 pp.

Johnson, D. E., P. K. Wang, and J. M. Straka (1993), Numerical simulations of the 2 August 1981 CCOPE supercell storm with and without ice microphysics, *J. Appl. Meteorol.*, *32*, 745–759.

Kain, J. S. (2004), The Kain–Fritsch convective parameterization: An update, *J. Appl. Meteorol.*, *43*, 170–181.

Kennedy, A. D., X. Dong, B. Xi, S. Xie, Y. Zhang, and J. Chen (2011), A comparison of MERRA and NARR eanalyses with the DOE ARM SGP data, *J. Climate*, *24*, 4541–4557.

Klazura, G. E., and D. A. Imy (1993), A description of the initial set of analysis products available from the NEXRAD WSR-88D system, *Bull. Am. Meteorol. Soc.*, *74*, 1293–1311.

Lang, S., W.-K. Tao, J. Simpson, and B. Ferrier (2003), Modeling of convective-stratiform precipitation processes: Sensitivity to partitioning methods, *J. Appl. Meteorol.*, *42*, 505–527.

Lang, S., W.-K. Tao, R. Cifelli, W. Olson, J. Halverson, S. Rutledge, and J. Simpson (2007), Improving simulations of convective systems from TRMM LBA: Easterly and westerly regimes, *J. Atmos. Sci.*, *64*, 1141–1164.

Lang, S., W.-K. Tao, X. Zeng, and Y. Li (2011), Reducing the biases in simulated radar reflectivities from a bulk microphysics scheme: Tropical convective systems, *J. Atmos. Sci.*, *68*, 2306–2320.

Leary, C. A., and R. A. Houze Jr. (1979), Melting and evaporation of hydrometeors in precipitation from the anvil clouds of deep tropical convection, *J. Atmos. Sci.*, *36*, 669–670.

Li, G., Y. Wang, K.-H. Lee, Y. Diao, and R. Zhang (2009), Impacts of aerosols on the development and precipitation of a mesoscale squall line, *J. Geophys. Res.*, *114*, D17205, doi:10.1029/2008JD011581.

Li, X., W.-K. Tao, A. P. Khain, J. Simpson, and D. E. Johnson (2009a), Sensitivity of a cloud-resolving model to bulk and explicit Bin microphysical schemes. Part I: Validation with a PRE-STORM case, *J. Atmos. Sci.*, *66*, 3–21.

Li, X., W.-K. Tao, A. P. Khain, J. Simpson, and D. E. Johnson (2009b), Sensitivity of a cloud-resolving model to bulk and explicit Bin microphysical schemes. Part II: Cloud microphysics and storm dynamics interactions, *J. Atmos. Sci.*, *66*, 22–40.

Lin, Y.-L., R. D. Farley, and H. D. Orville (1983), Bulk parameterization of the snow field in a cloud model, *J. Clim. Appl. Meteorol.*, *22*, 1065–1092.

Luo, Y., Y. Wang, H. Wang, Y. Zheng, and H. Morrison (2010), Modeling convective-stratiform precipitation processes on a Mei-Yu front with the weather research and forecasting model: Comparison with observations and sensitivity to cloud microphysics parameterizations, *J. Geophys. Res.*, *115*, D18117, doi:10.1029/2010JD013873.

McCumber, M., W.-K. Tao, J. Simpson, R. Penc, and S.-T. Soong (1991), Comparison of ice-phase microphysical parameterization schemes using numerical simulations of tropical convection, *J. Appl. Meteorol.*, *30*, 985–1004.

Mesinger, F., et al. (2006), North American regional reanalysis, *Bull. Am. Meteorol. Soc.*, *87*, 343–360.

Mlawer, E. J., S. J. Taubman, P. D. Brown, M. J. Iacono, and S. A. Clough (1997), Radiative transfer for inhomogeneous atmosphere: RRTM, a validated correlated-k model for the longwave, *J. Geophys. Res.*, *102*(D14), 16,663–16,682.

Morrison, H., and A. Gettelman (2008), A new two-moment bulk stratiform cloud microphysics scheme in the community atmosphere model,

version 3 (CAM3). Part I: Description and numerical tests, *J. Climate*, *21*, 3642–3659.

Morrison, H., G. Thompson, and V. Tatarskii (2009), Impact of cloud microphysics on the development of trailing stratiform precipitation in a simulated squall line: Comparison of one- and two-moment schemes, *Mon. Weather Rev.*, *137*, 991–1007.

Proctor, F. H. (1988), Numerical simulations of an isolated microburst. Part I: Dynamics and structure, *J. Atmos. Sci.*, *45*, 3137–3160.

Proctor, F. H. (1989), Numerical simulations of an isolated microburst. Part II: Sensitivity experiments, *J. Atmos. Sci.*, *46*, 2143–2165.

Rutledge, S. A., and P. V. Hobbs (1983), The mesoscale and microscale structure and organization of clouds and precipitation in midlatitude cyclones. Part VIII: A model for the "seeder feeder" process in warm-frontal rainbands, *J. Atmos. Sci.*, *40*, 1185–1206.

Skamarock, W. C., J. B. Klemp, J. Dudhia, D. O. Gill, D. M. Barker, M. G. Duda, X.-Y. Huang, W. Wang, and J. G. Powers (2008), A description of the advanced research WRF version 3, *NCAR Technical Note*.

Steiner, M., R. A. Houze Jr., and S. E. Yuter (1995), Climatological characterization of three-dimensional storm structure from operational radar and rain gauge data, *J. Appl. Meteorol.*, *34*, 1978–2007.

Straka, J. M., and J. R. Anderson (1993), Numerical simulations of microburst-producing storms: some results from storms observed during COHMEX, *J. Atmos. Sci.*, *50*, 1329–1348.

Tao, W.-K., and J. Simpson (1993), Goddard cumulus ensemble model. Part I: Model description, *Terr. Atmos. Oceanic Sci.*, *4*, 35–72.

Tao, W.-K., J. Simpson, and M. McCumber (1989), An ice-water saturation adjustment, *Mon. Weather Rev.*, *117*, 231–235.

Tao, W.-K., X. Li, A. Khain, T. Matsui, S. Lang, and J. Simpson (2007), Role of atmospheric aerosol concentration on deep convective precipitation: Cloud-resolving model simulations, *J. Geophys. Res.*, *112*, D24S18, doi:10.1029/2007JD008728.

Varble, A., A. Fridlind, E. J. Zipser, A. Ackerman, J. P. Chaboureau, J. Fan, A. Hill, S. A. McFarlane, J. P. Pinty, and B. Shipway (2011), Evaluation of cloud-resolving model intercomparison simulations using TWP-ICE observations: Precipitation and cloud structure, *J. Geophys. Res.*, *116*, D12206, doi:10.1029/2010JD015180.

Yuter, S. E., and R. A. Houze Jr. (1995), Three-dimensional kinematic and microphysical evolution of Florida cumulonimbus. Part II: Frequency distributions of vertical velocity, reflectivity, and differential reflectivity, *Mon. Weather Rev.*, *123*, 1941–1963.